Uncertainties in Oceanic Radar Rain Maps at Kwajalein and Implications for Satellite Validation

Robert A. Houze Jr., Stacy Brodzik, Courtney Schumacher, and Sandra E. Yuter

University of Washington, Seattle, Washington

Christopher R. Williams

Cooperative Institute for Research in Environmental Sciences, University of Colorado, and NOAA Aeronomy Laboratory, Boulder, Colorado

ABSTRACT

The Kwajalein, Marshall Islands, Tropical Rainfall Measuring Mission (TRMM) ground validation radar has provided a multiyear three-dimensional radar dataset at an oceanic site. Extensive rain gauge networks are not feasible over the ocean and, hence, are not available to aid in calibrating the radar or determining a conversion from reflectivity to rain rate. This paper describes methods used to ensure the calibration and allow the computation of quantitative rain maps from the radar data without the aid of rain gauges. Calibration adjustments are made by comparison with the TRMM satelliteborne precipitation radar. The additional steps required to convert the calibrated reflectivity to rain maps are the following: correction for the vertical profile of reflectivity below the lowest elevation angle using climatological convective and stratiform reflectivity profiles; conversion of reflectivity (Z) to rain rate (R) with a relationship based on disdrometer data collected at Kwajalein, and a gap-filling estimate. The time series of rain maps computed by these procedures include low, best, and high estimates to frame the estimated overall uncertainty in the radar rain estimation. The greatest uncertainty of the rain maps lies in the calibration of the radar ($\pm 30\%$). The estimation of the low-altitude vertical profile of reflectivity is also a major uncertainty ($\pm 15\%$). The Z–R and data-gap uncertainties are relatively minor ($\pm 5\%$ or less). These uncertainties help to prioritize the issues that need to be addressed to improve quantitative rainfall mapping over the ocean and provide useful bounds when comparing radar-derived rain estimates with other remotely sensed measures of oceanic rain (such as from satellite passive microwave sensors).

1. Introduction

Measuring and mapping rainfall over the oceans are two of the major challenges of the atmospheric sciences. Over much of the ocean we rely on remote sensing by satellites. For over 20 years, passive microwave radiometry and infrared-based methods have been the principal avenues for detecting precipitation from space (Stephens 1994; Kidder and Vonder Haar 1995). Because most meteorological radars and rain gauges are on land, the data available for validating satellite rain retrievals over the ocean are extremely sparse. One of the accomplishments of the Tropical Rainfall Measuring Mission (TRMM; Simpson et al. 1988; Kummerow et al. 1998) has been the establishment of a tropical oceanic ground validation site at the Kwajalein atoll in the Marshall Islands of the western tropical Pacific Ocean.

Kwajalein is a suitable location for validating rainfall detection from space. The atoll is in a rainy location on the northern edge of the Pacific intertropical convergence zone (ITCZ). Because of this location on the edge of the ITCZ, Kwajalein receives rain from a wide variety of oceanic tropical convection. Schumacher and Houze (2003a,b) show that not only does Kwajalein receive moderately frequent rain from convective systems with large stratiform rain components, it also has a large population of isolated shallow ($<\sim 5$ km deep) precipitating convection. Approximately 1900 mm of rain falls in the vicinity of the atoll during a typical year. The rain falls mostly from July to December, when the ITCZ is farthest north. Because of Kwajalein's position on the northern edge of the ITCZ, the rain amounts decrease from ~ 2500 mm south of the atoll to ~ 1300 mm over the atoll region itself. The primary instrument at the Kwajalein site is a 10-cm-wavelength (S band) radar (Table 1). The atoll has such a small landmass that the area surveyed by the radar is essentially all oceanic (Figs. 1 and 2). This 360° ocean view makes the site ideal for validation of the emission-based passive microwave techniques used over oceans (Wilheit et al. 1977; Wilheit 1986).
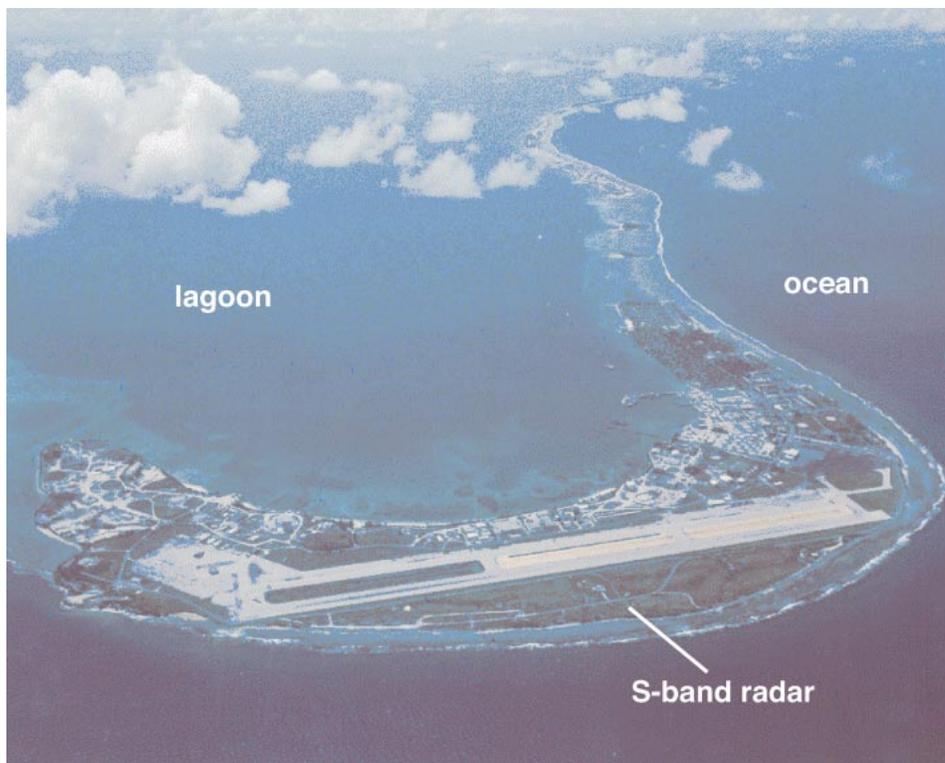
FIG. 1. Areal view of the Kwajalein radar site. The width of Kwajalein Island is on the order of a few hundred meters, making the area surveyed by the radar almost entirely oceanic.

Over land, rain gauges can be used to monitor radar calibration (Joss et al. 1998). However, the small (and largely inaccessible) land surface of the Kwajalein atoll precludes the deployment of a large network of rain gauges. Therefore, special techniques have been necessary to make the Kwajalein radar a satisfactory ground validation instrument. This paper describes these techniques, which include calibration adjustment based on the TRMM precipitation radar (PR) correction for the vertical profile of reflectivity below the lowest elevation angle, using climatological convective and stratiform reflectivity profiles; conversion of reflectivity (Z) to rain rate (R) with a relationship based on disdrometer data collected at Kwajalein; and a gap-filling estimate. The

TABLE 1. Characteristics of the Kwajalein radar.

Characteristic	Value
Frequency/wavelength	2.8 GHz/10.71 cm (S band)
Beamwidth	1.12°
Peak transmit power	500 kW (250 kW horizontal and vertical)
Pulse duration	0.8 μs
Minimum detectable signal	-108 dBm
Doppler	Yes
PRF	396–960 Hz
Antenna height MSL	24.8 m
Speed of one scan	360° in 22.5 s (max)
Scan range	$-0.4°$ to 90.5° (elevation)
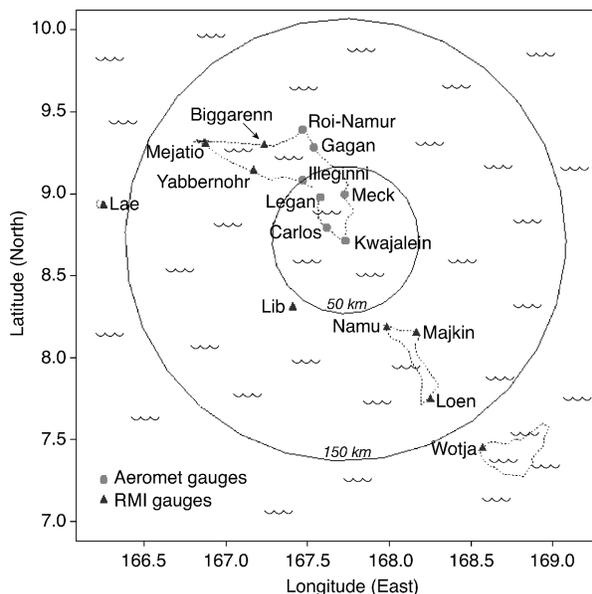
FIG. 2. Area covered by the Kwajalein radar. The 150-km-range circle is the outer edge of the Kwajalein rain maps described in this paper. Dotted lines indicate the chains of small islands surrounding the three major lagoons in the region. Note that water lies inside as well as outside of each of the island chains so that >99% of the area surveyed by the radar is ocean. Note also that the rain gauge locations are restricted to the islands, many of which are inaccessible.

few rain gauges on the atoll serve as a check on the methodology; however, the methodology does not depend on the gauges. These techniques guarantee that the entire three-dimensional reflectivity field (as opposed to only the surface rain maps) is calibrated. In addition, they allow us to isolate the separate sources of error in the radar rain maps (radar calibration, the change of reflectivity with height, drop size distribution variations, and data gaps), which allows the assessment of the relative uncertainties from each component. We demonstrate the use of the rain maps and uncertainty estimates as a validation product by comparing them with the TRMM Microwave Imager (TMI) precipitation maps to determine the degree of agreement between the ground validation data at Kwajalein and the TRMM passive microwave sensor.

2. The University of Washington Kwajalein product set

The U.S. Army Kwajalein Missile Range has maintained a weather station for over 50 years. A private contractor, Aeromet, Inc., operated the station during most of the TRMM time frame and for the entire period covered by this study. In 1996, the National Aeronautics and Space Administration (NASA) updated the weather radar at Kwajalein with the S-band radar formerly operated by the National Center for Atmospheric Research (NCAR) as the "Mile High Radar" (Table 1). The University of Washington (UW) helped to develop the rainfall maps derived from the Kwajalein ground validation site. A set of rain maps computed and archived for Kwajalein by the TRMM Satellite Validation Office is available through the Goddard Space Flight Center's Distributed Active Archive Center (DAAC; available online at http://lake. nascom.nasa.gov/data/dataset/TRMM/01_Data_Products/ 03_Ground_Instruments/KWAJ/). For several years, UW has computed and archived a similar set of products as a research project aimed at improving the techniques used in mapping the Kwajalein rainfall, which are also available through the DAAC (online at http://lake.nascom. nasa.gov/data/dataset/TRMM/01_Data_Products/ 03_Ground_Instruments/UW_KWAJ). The UW products differ from the TRMM Satellite Validation Office products in several respects. In particular, the TRMM Satellite Validation Office originally used rain gauges to tune their rain maps. Recently, the Satellite Validation Office has adopted a procedure more similar to the one promoted in this paper; however, it still does not incorporate quantitative estimates of the uncertainty in the ground validation products (Marks et al. 2000). These uncertainty estimates are the focus of this paper.

Figure 3 shows the steps in converting the Kwajalein radar (KR) data to the UW Kwajalein ground validation products, which are archived at the DAAC. The radar data are processed using the SIGMET, Inc., RVP7 processor. We refer to the polar coordinate output of this
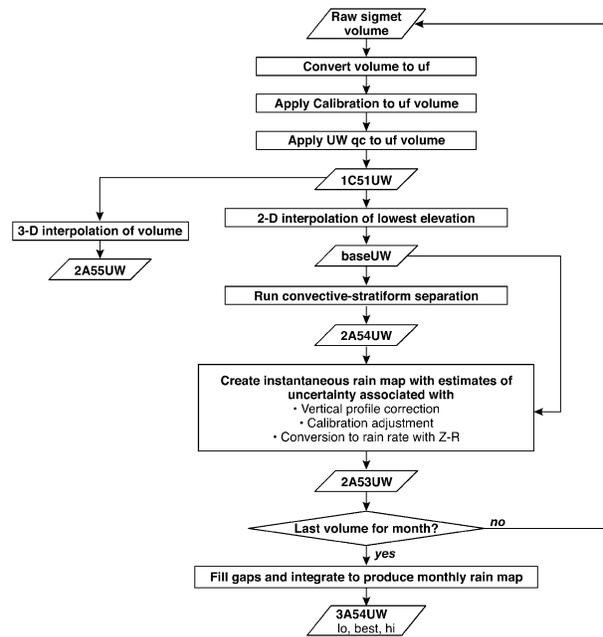
FIG. 3. Flowchart of processing Kwajalein radar data to produce monthly rain maps. See text for explanation.

processor as the sigmet files. These data are processed to a maximum range of 150 km, which is a typical maximum distance from the radar for quantitative rain estimation. The sigmet data are converted to universal format (uf; Barnes 1980) and we apply a calibration correction to the uf file, as discussed in section 3. We then apply a quality-control (QC) algorithm developed at the UW to the uf data to remove sea clutter, the second-trip echo, and anomalous propagation (see the appendix). The latter artifact is usually not present at Kwajalein, but sea clutter and second-trip echoes are frequent. The end product of the processing through the QC stage is called 1C51UW. This naming follows the NASA TRMM convention (described online at http:// trmm.gsfc.nasa.gov/gvoverview.html). A level-1 product is a raw but quality-controlled dataset. Product names starting with a 2 are *derived* from the raw data obtained *at a given time*. Level-3 products are those integrated over 1 month. Our experimental products archived at the DAAC carry the UW suffix to distinguish them from the TRMM Satellite Validation Office products.

The 1C51UW product is in radar coordinates (azimuth, elevation, and range). We interpolate each volume to a Cartesian grid using the widely available NCAR "SPRINT" software (Mohr and Vaughan 1979). Three-dimensional interpolation leads to the product 2A55UW, which is the calibration-corrected three-dimensional reflectivity field on a Cartesian grid (2-km horizontal and 1-km vertical resolutions). Two-dimensional interpolation of the lowest elevation angle data leads to a Cartesian base map of the reflectivity field nearest the ocean

surface at 2-km horizontal resolution (baseUW). We archive this product at the DAAC because it is more closely related to the rainfall at the surface than is the lowest altitude level in product 2A55, for which the lowest level is a constant altitude based partly on data from elevation angles above the lowest elevation angle.

The Cartesian base map of reflectivity (baseUW) is separated into convective and stratiform components using a texture-based algorithm conceived by Churchill and Houze (1984) and refined for use in TRMM products by Steiner et al. (1995) and Yuter and Houze (1997). The result is a base-map Cartesian field showing whether each pixel of reflectivity is part of a convective or stratiform region (2A54UW). The TRMM Satellite Validation Office 2A54 algorithm is also based on Steiner et al. (1995).

The baseUW and 2A54UW maps serve as input to product 2A53UW, which is our instantaneous rain map. We perform three processes to convert the reflectivity data to a rain map. First, we correct the reflectivity at every rainy pixel to account for the probable vertical profile of reflectivity below the lowest observed elevation. We extrapolate downward empirically by a method discussed in section 5. We make a best estimate and estimate the range of uncertainty in the downward extrapolation. Second, we estimate the uncertainty in the reflectivity owing to uncertainty in the calibration adjustment applied in the creation of 1C51UW (section 4). Third, we convert the surface reflectivity at each pixel to rain rate by a Z–R relationship based on disdrometer data at Kwajalein (section 6). The disdrometer data are also used to indicate the upper and lower bounds of uncertainty in the rain rate. Much of this paper (sections 3–6) is concerned with the details of these three processing steps leading to the 2A53UW product.

After rain maps (2A53UW) have been determined for a whole month, they are combined to form the monthly rain map, product 3A54UW. When we integrate the instantaneous rain maps over a whole month, we integrate the low-, best-, and high-estimate maps to obtain monthly lower-limit, best-estimate, and high-estimate maps. When we integrate the instantaneous maps over the whole month we fill data gaps by the method discussed in section 7. Our gap-filling procedure also makes a best estimate, lower limit, and upper limit for each gap. The final 3A54UW product consists of a best-estimate map accompanied by low- and high-estimate maps associated with each of the four sources of uncertainty: calibration, the vertical profile of reflectivity below the lowest scan, the Z–R relationship, and gap filling. Each of these nine maps consists of a network common data form (netCDF) file on a 151×151 grid of 2-km square pixels. The low- and high-estimate maps included in the 3A54UW product constitute the error bars for the best-estimate maps contained in that product.

The four distinct types of uncertainty identified in our rain map product sets are often combined into a single Z–R relationship. We choose to separate them, because

they are independent sources of error. The calibration error is a bias with no random error (calibration error is generally constant for a given radar volume). The vertical profile of reflectivity below the lowest beam of the radar depends on precipitation type and atmospheric conditions, and has a bias and random error. The variation in the drop spectrum also has a bias and a random component. Data gaps introduce a negative bias. By separating the sources of error, we help the user understand how to interpret the data, and we obtain a more clear indication of where improvements are needed. Sections 3–6 describe how we obtain the best-, low-, and high-estimate rain maps for each category of uncertainty.

3. Calibration correction

a. TRMM PR as a stable standard

The calibration of a meteorological radar should be monitored against a stable standard. Over land, a network of several hundred rain gauges can serve as a calibration standard (Joss et al. 1998). At Kwajalein, such a network is logistically impractical to install. Over 99% of the area surveyed by the radar is ocean. Most of the islands in the atoll have a smaller area than an individual radar pixel, and only a few of the islands are sufficiently large as to be not awash with seawater during storms. Data from the approximately 5–10 rain gauge–radar pixel pairs usually available from the atoll region, are inadequate for statistical monitoring of the calibration. Therefore, some other standard is required. The PR aboard the TRMM satellite is a consistently available comparison standard for the KR. The calibration of the PR reflectivity is constant and is thought to have an accuracy of about ± 1 dB (Kummerow et al. 1998; Kozu et al. 2001). We do not use a product derived from the reflectivity (such as PR rain rate) because that type of product is subject to change from one version of the TRMM product set to the next. As long as the TRMM satellite is in orbit it will serve as a standard for the KR. When the Global Precipitation Measurement (GPM) satellite system is in place later in this decade, the radar aboard the main satellite can take over as the calibration standard for Kwajalein. Thus, a satellite-borne radar will be available as a calibration standard for many years.

b. Calibration adjustment based on matching echo area

The calibration adjustments that we have applied to the KR data are obtained by a simple area-matching method (Schumacher and Houze 2000). This approach is an after-the-fact method for determining the gross calibration changes that have occurred at Kwajalein since the TRMM launch in November 1997. We compare the area covered by echo by the KR with the

TABLE 2. Kwajalein radar calibration corrections. Changes of radar status include some that may not be directly related to radar calibration, such as the beginning of the data archive, maintenance of the azimuth and elevation motors, and changes in scan strategy. These items further help to define the time periods when particular calibration corrections are applied.

Time period	Change of radar status	Calibration correction (dB)
5 Aug–13 Oct 1998	5 Aug 1998: Archive began	+4
22 Oct–28 Dec 1998	12–21 Oct 1998: Azimuth motor replacement	0
10 Jan–19 May 1999	28 Dec 1998–9 Jan 1999: Transmitter diode replacement	+1
20 May–21 Jun 1999	19 May 1999: Pulse filament transformer replacement	KR questionable
22 Jun 1999–5 Apr 2000	21 Jun 1999: Separate V channel installed, polarization switch removed, pulse burst aligned, stalo adjusted	+6
6 Apr–1 May 2000	6 Apr 2000: Azimuth belt maintenance	+3
2 May–21 Aug 2000	Unknown	0
22 Aug–25 Sep 2000	21 Aug 2000: Pulse-forming network (PFN) replacement	−3
26 Sep–22 Oct 2000	25 Sep 2000: Scanning strategy changed	−1
23 Oct–20 Nov 2000	22 Oct 2000: Pulse transformer failed	0
21 Nov–12 Dec 2000	19 Nov 2000: PFN replacement	−3
13 Dec 2000–6 Aug 2001	12 Dec 2000: PFN replacement	+1
7–24 Aug 2001	Orbit adjustment	Not available
25 Aug–2 Dec 2001	25 Aug 2001: PR data unstable	PR questionable
3 Dec 2001–3 May 2002	3 Dec 2001: PR data became stable	+6

TRMM PR 2A25 product (three-dimensional gridded attenuation-corrected reflectivity; Iguchi et al. 2000). To do this, we reinterpolate the 1C51UW product (Fig. 3) to a 4 km × 4 km horizontal grid to compare with the PR data obtained prior to the orbital elevation increase in August 2001 to match approximately the horizontal resolution of the PR data in the 2A25 product. For data collected after August 2001, we interpolate the KR data to a 5 km × 5 km grid to approximate the PR resolution after the satellite's altitude boost. The simplicity of our approach lies in the fact that we take the gridded PR data (2A25) at face value and perform a standard interpolation program to the KR data. Much time is saved by not processing the satellite data.

A basic premise of the area-matching technique is that any dBZ calibration correction is an additive value that is a constant across the field of view of the radar. Therefore, regardless of how the corrective value is determined, the final result must produce an echo area that agrees with the area of echo seen by the PR. We determine a calibration correction by seeking the dBZ correction required to make the area covered by echo seen by the KR at reflectivity >17 dBZ (sensitivity of the PR) at the 6-km level (ice region) most closely match the area of echo >17 dBZ with the reflectivity values seen by the PR at the same level. We call this dBZ correction the *calibration offset*. We choose a lower reflectivity threshold value (17 dBZ) because higher reflectivity values are subject to attenuation at the PR wavelength (~2 cm). Steiner and Houze (1998) pointed out that the reflectivity differences in the 5–7-km layer are the best indication of instrumental calibration offset because these levels lie above the melting layer and

above strong convective cores so that they are not subject to attenuation, and they are sufficiently far below the echo top that the sample size is reasonable. This area–coverage comparison is simple to apply and uses the entire overlap of coverage of the PR and KR.

The calibration offsets determined by our area-matching technique are indicated in Table 2 and Fig. 4a. From the TRMM launch in November 1997 to August 1998, Kwajalein experienced a drought; therefore, the useful record starts with August 1998. Periods of obvious large bias are evident in Fig. 4a. Each period of bias delineated by the vertical lines started abruptly in association with a particular instrumental problem (Table 2, middle column). The last column of Table 2 lists the calibration correction required to obtain maximum consistency between the KR and the PR. Figure 4b shows the difference in the area covered by echos between the two radars after applying this bias correction to the data in Fig. 4a. The corrections bring the time series of the KR in line with the PR until the satellite's orbit boost in August 2001. After that month, the KR and PR differences become erratic and cannot be brought in line for the rainy season months of 2001. Sensitivity tests show that the results from the area-matching method do not change if the threshold is increased to 20 dBZ or if data only within 100 km are used in the calculation.

Figure 5 shows the time series of monthly rainfall based on the Kwajalein radar for the period of July 1999–August 2001, a period when the radar data were uninterrupted but underwent several significant calibration corrections according to Table 2 and Fig. 4. The two curves indicating the monthly totals before and after our calibration corrections are applied. This figure in-
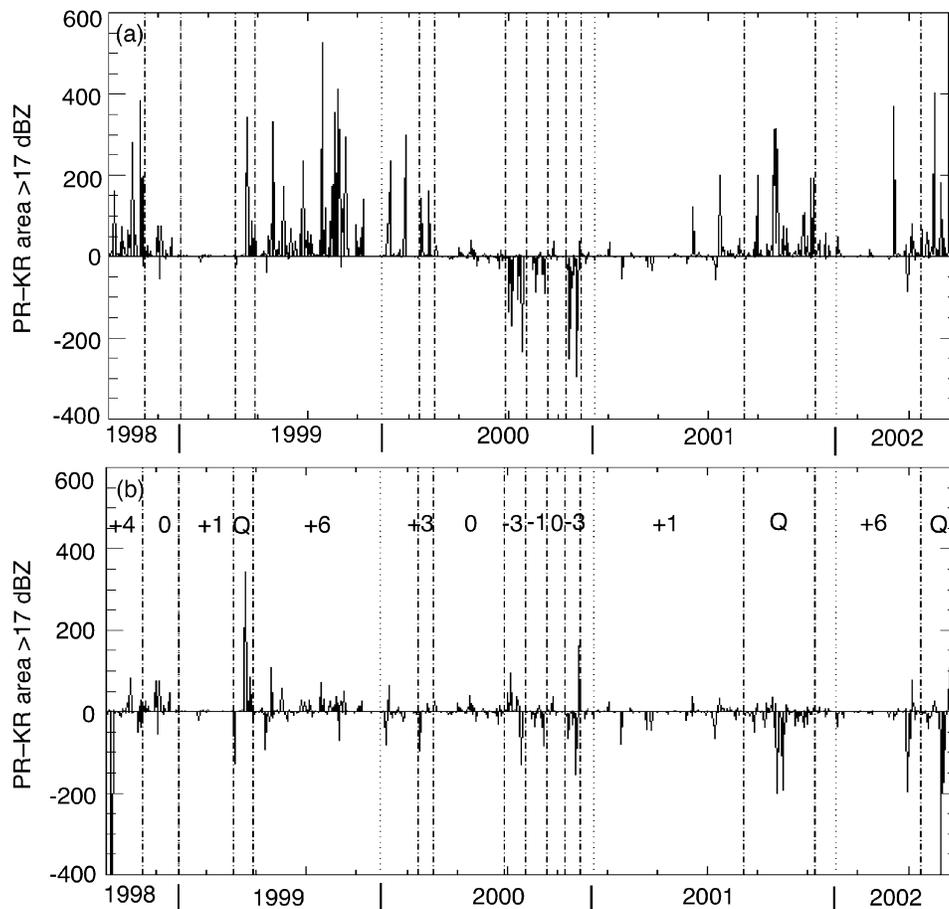
FIG. 4. (a) Difference between area covered by reflectivity >17 dBZ as seen by the TRMM PR and the KR each time the PR swath intersected the KR radar area. (b) Same as (a) after the indicated calibration adjustments (dB) have been applied; Q indicates that one of the radars had questionable data quality.

dicates the impact of the calibration corrections on the total rainfall estimates for Kwajalein.

4. Comparison of calibration corrections obtained by different methods

Bolen and Chandrasekar (2000, hereinafter BC00) and Anagnostou et al. (2001) have also developed methods for comparing the KR and PR. Both studies interpolate spatially in a very precise manner and compare mean reflectivity at a series of altitudes. These procedures require reinterpolation of the satellite radar data as well as the KR data. This section seeks answers to the following two questions: *(i) Is there a measurable advantage to a detailed two-radar interpolation and precise spatial alignment? (ii) Does a better calibration correction come from echo area matching or matching of the mean reflectivity?*

a. Spatial interpolation

BC00 and Anagnostou et al. (2001) interpolate both the satellite and ground radar data after making a precise

spatial alignment of the three-dimensional reflectivity fields from the KR and PR. This intensive interpolation has the advantage of having maximum precision in space. However, it has the disadvantages of being computationally intensive and labor intensive. In addition, the precision in space may be unnecessary in view of the lack of precision in time. The ground radar volume is obtained over a 5–10-min period as the antenna scans from lower to upper elevation angles. Because the satellite sample is essentially instantaneous, PR and KR data will always be off in time by a few minutes.

To examine the importance of the interpolation method, we employed the BC00 method on 64 TRMM orbital overpasses of Kwajalein between August 1998 and August 2001 (see Table 3, BC00's 64 orbits).[1] Radar echo in at least one 50 km × 50 km area was examined in each orbit. Each 50 km × 50 km box required one calculation using the BC00 software. An analyst had to

---

[1] We note that the version of the BC00 method applied in this paper uses the 1C21 product (not corrected for attenuation) as the PR input dataset.
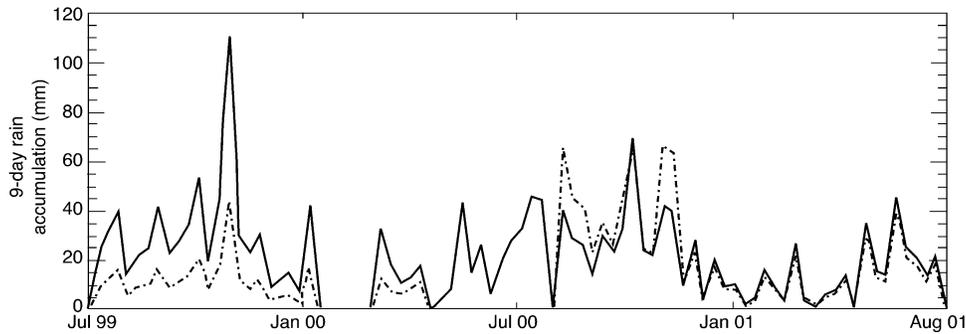
Fig. 5. Time series of 9-day rain accumulations computed from Kwajalein radar with (solid) and without (dashed) calibration correction.

examine the PR and KR imagery and select a 50 km × 50 km echo area that appeared to offer a substantial amount of area covered by echo and, hence, a statistically meaningful comparison. The box also had to lie within 100 km of both the KR radar and the TRMM ground track of the subsatellite point to maximize the vertical resolution of the two interpolated reflectivity fields. On some of the orbits we examined multiple 50 km × 50 km boxes for sufficient echo meeting these requirements. Altogether 149 50 km × 50 km boxes were examined. This process required much human intervention and numerous subjective decisions.

A subset of the UW dataset was obtained for the same 64 orbits used in the BC00 calculations (see Table 3, UW's 64 orbits). However, UW's 64-orbit subset is not restricted to the 50 km × 50 km boxes of the BC00 method, but rather uses the whole overpass swath overlapping the Kwajalein radar. The total number of pixels in UW's 64-orbit calculation is reduced as compared with the total number of overpasses (see Table 3, UW's 562 orbits) from 22 353 to 10 742 (a factor-of-2 reduction in sample size). Because it is restricted to selected 50 km × 50 km boxes, the BC00 64 orbits calculation is performed on a still smaller sample size of 4550 pixels (a factor-of-5 reduction in comparison with UW's 562-orbit calculation).

Figure 6a shows the frequency distribution of echo >17 dBZ at 6 km for the overlap areas of the KR and PR for the orbits used in BC00's 64- and UW's 64-orbit calculations. Two major differences are apparent from Fig. 6. First, the KR sees more high reflectivity than the PR at 6 km; second, the BC00 method sees more high reflectivity than the UW method.

The first difference is largely the result of the interpolation of the KR aliasing high reflectivity from below 6 km into the pixels at 6-km altitude. The high reflectivity could be associated with bright bands or convective cores of reflectivity below the 6-km level. With its 250-m range resolution, and its quasi–vertically pointing viewing geometry, the PR is more likely (in the absence of attenuation) to see the true reflectivity at 6 km. Examination of the reflectivity distributions at higher altitudes show that the difference between the PR and

KR decreases with height, which is consistent with this assessment. As an additional test, the UW dataset was restricted to data within a 100-km radius of the KR, which should reduce the effect of beamwidth widening and the inclusion of reflectivity below 6 km. However, the KR distributions changed very little with this reduction of spatial domain (Fig. 6b). Thus, the aliasing appears to be unavoidable.

The second difference is likely due to the fact that the boxes used in the BC00 calculations were subjectively selected because they contained echoes that were large and/or intense. Therefore, the reflectivity distributions would be expected to contain proportionally more high-reflectivity echoes than the UW method, which includes all the echoes present in a given volume. It would be possible to repeat BC00's selection process until all the echoes present were accounted for. Eventually, the BC00 KR histogram might come into line with the UW KR histogram. However, this additional processing only further increases the time commitment of the technique. Based on the reflectivity distributions in Fig. 6, there does not appear to be a measurable advantage to a sophisticated and time-consuming interpolation when looking at many volumes of data.

b. Echo area matching versus difference of mean reflectivity

The UW method uses the echo area–matching method to determine the calibration offset (section 3b), while BC00 determines the calibration offset by taking the difference of the mean reflectivity between the PR and KR at a selected height. The calibration offsets from both methods for the 64 orbits are listed in the right-hand portion of Table 3. In addition, the results of the UW interpolation and area matching for all 562 orbits are listed in the columns labeled UW's 562 orbits. These results are directly from Table 2. In Table 2 there are time periods when orbits are not interpolated using the BC00 method, and these time periods are not included in the 562-orbit column of Table 3. Most of the data in Table 2 are included in the 562-orbit dataset.

The columns labeled "area match calibration" in Ta-

TABLE 3. Calibration statistics from 562 orbits shown in Table 2 and for the 64-orbit subset used for comparing the mean difference (BC00) and matching (UW) methods.

	562-orbit UW interpolation			64-orbit UW interpolation				64-orbit BC00 interpolation		
Date	No. orbits	No. PR pixels	Area match calibration (dB)	No. orbits	No. PR pixels	Mean diff calibration (dB)	Area match calibration (dB)	No. PR pixels	Mean diff calibration (dB)	Area match calibration (dB)
5 Aug–13 Oct 1998	36	2208	+4	6	1500	0.3	+3	1336	−1.6	+3
22 Oct–28 Dec 1998	37	898	0	6	302	−0.4	+2	278	−2.5	+1
22 Jun 1999–5 Apr 2000	164	6230	+6	8	1786	1.8	+7	637	0.5	+6
6 Apr–1 May 2000	15	900	+3	1	296	1.3	+4	115	3.0	+4
2 May–21 Aug 2000	71	2688	0	14	1253	−0.9	+1	644	−1.8	+1
22 Aug–25 Sep 2000	22	1235	−3	5	772	−1.8	−1	271	−6.1	−5
26 Sep–22 Oct 2000	20	773	−1	2	151	−4.0	−2	76	−5.5	−3
23 Oct–20 Nov 2000	18	387	0	3	272	−1.7	+1	109	−1.2	+1
21 Nov–12 Dec 2000	16	2411	−3	4	790	−2.6	−2	327	−7.0	−4
13 Dec 2000–6 Aug 2001	163	4623	+1	15	3620	−1.6	+1	757	−3.4	−1
Tot Avg	562	22 353	1	64	10 742	−1.0	1.4	4550	−2.3	0.3

ble 3 indicate that all three datasets yield similar calibration adjustments by the area-matching technique. Thus, the interpolation method does not seem to affect the determination of the calibration offset.

In the UW and BC00 64-orbit calculations we computed a possible calibration adjustment based on the difference between the mean PR and mean KR reflectivity at the 6-km level. (All mean reflectivities are computed in Z, and the calibration differences are obtained by subtracting the dBZ of the KR mean from the dBZ value of the PR mean.) Table 3 shows that in the UW 64 orbits calculations the values are mostly negative, averaging to a value of −1.0 dB, in contrast to the area-matching calibration correction average of +1.4 dB. In BC00's 64 orbits the averages for the mean difference and area-matching corrections are −2.3 and +0.3 dB, respectively. Again, the interpolation method does not appear to affect the determination of the calibration offset. However, the calibration adjustments implied by the mean difference method are generally negative in the Kwajalein dataset and are generally positive when using the area-matching method.

If there were no differences between the shapes of the distributions, the area-matching and difference-of-means methods would give the same calibration offset. Figure 6, however, indicates how easily the shape of the reflectivity distributions seen by the PR and KR can differ as a result of scanning geometry. The mean difference correction is sensitive to the histogram shape, and application of the mean difference corrections in the present case would lead to vastly inconsistent areas of echo coverage on the PR and KR, an unacceptable result; this conclusion is easily inferred from inspection of Fig. 4a. The area-matching method is relatively insensitive to the histogram shape and, thus, less prone to error.

5. Calibration uncertainty

The calibration corrections in Table 2 remove the major part of the calibration bias associated with changes in the status of the radar equipment. Our best-estimate rain maps are computed using the calibration corrections; however, after the gross calibration correction has been made according to Table 2, an uncertainty remains.

The basic operation of the radar is monitored by standard methods. Aeromet makes daily measurements of the transmitter performance (peak power, modulator current, and magnetron current) and of servo performance. They also make antenna gain and alignment measurements using a solar scan measurement technique to monitor the performance of the receiver and the antenna. A receiver calibration is performed about once a month by putting known power levels into the system with a signal generator. Sphere calibrations have proved unfeasible because of typically strong winds. A standard gain horn calibration has been performed as part of the comprehensive radar hardware assessments
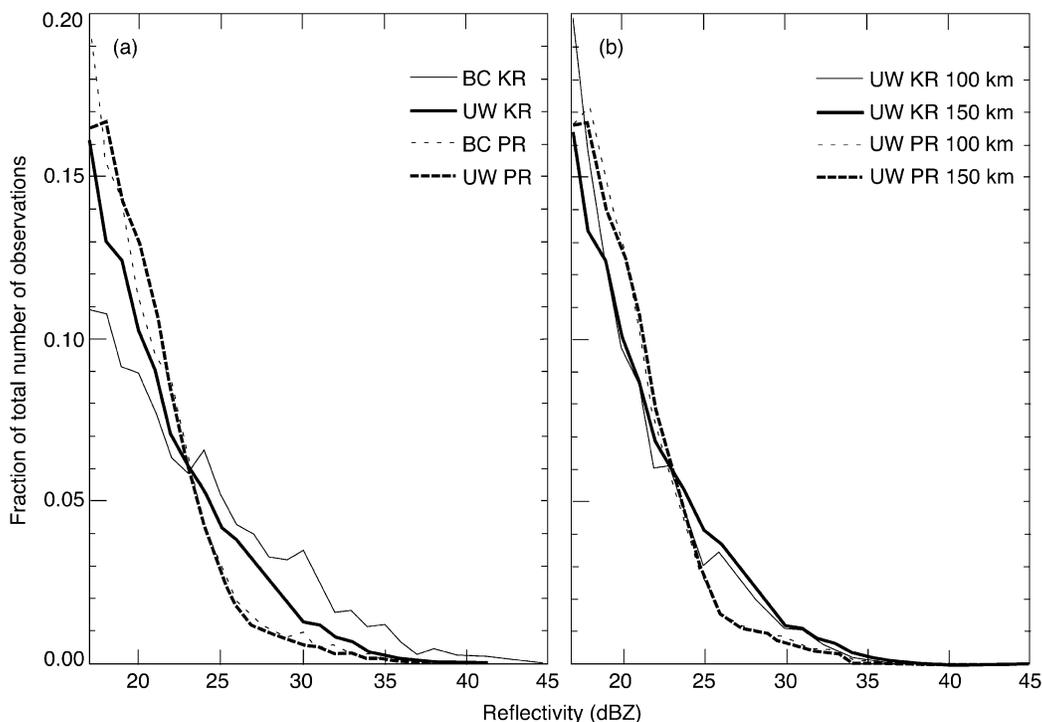
FIG. 6. Frequency distributions of radar reflectivity at 6 km observed in the 64-orbit subset described in the text: (a) comparison of BC00 and UW methods; (b) comparison of UW results for two different domain sizes.

in October 1999, March 2000, and March 2001. Given these measurements, a conservative (rather than optimistic) estimate of typical hardware calibration uncertainty at Kwajalein is ~2 dB (P. Smith, E. Mueller, and V. Chandrasekar 2000, personal communication). This uncertainty is consistent with the magnitudes of the estimated calibration corrections in Table 2, which suggest that the instrumental calibration of the KR has undergone sporadic changes on the order of a few decibels.
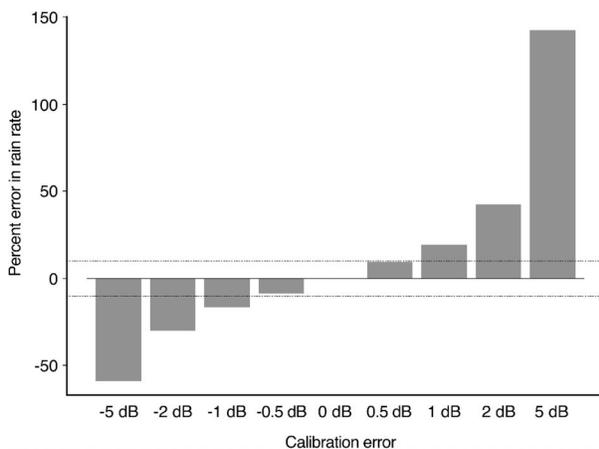
FIG. 7. Percent error in rain rate for different assumed calibration errors in radar reflectivity. Numbers are based on the Z–R relation derived from disdrometer data taken at Kwajalein in 1999–2000. The dotted lines are for a 10% error.

Section 7 describes a Z–R relation derived from disdrometer data collected at Kwajalein during the 1999 and 2000 rainy seasons. We use this relation to determine the uncertainty in rain rate associated with the apparent calibration uncertainty of ± 2 dB. The best-estimate Z–R relation derived from the disdrometer dataset is used to calculate $[R(\mathrm{dB}Z \pm 2)/R(\mathrm{dB}Z)] \times 100\%$. This calculation yields the percentage error for reflectivity under- and overestimated by 2 dB. The percentages are 130% for $\mathrm{dB}Z + 2$ and 70% for $\mathrm{dB}Z - 2$. On the basis of these results, we obtain high- and low-estimate maps by multiplying the best-estimate pixels by 1.3 and 0.7, respectively. This uncertainty is a major factor in the overall uncertainty of the rain maps. The bar graph in Fig. 7 shows the percent error in rain rate associated with a given error in reflectivity. To achieve a 10% uncertainty in rain rate, the absolute calibration would have to be ± 0.5 dBZ. One of the ongoing objectives of the Kwajalein ground validation site is to improve the calibration to this level. Such improvement could be possible with various hardware and software improvements at the site.

6. Vertical profile uncertainty

One of the principal uncertainties in estimating surface rain rate from the radar is the change in reflectivity with height below the lowest beam of the radar (Joss and Waldvogel 1990; Vignal et al. 2000). The drop size

TABLE 4. Modal values of reflectivity difference between the mean height and the 0.5-km level. Based on data from all TMI overpasses between Aug 1998 and Jan 2001.

Beam height (km)	Diff between reflectivity and 0.5 km and the reflectivity at beam height	
	Convective	Stratiform
2.5	3.06	0.25
2.0	2.31	0.44
1.5	1.54	0.49
1.0	0.82	0.46

spectrum continues to evolve by coalescence, breakup, and sedimentation below the lowest elevation angle. This effect becomes greater with increasing range, because the beam tilts upward relative to the surface of the earth. The height of the $0.4°$ beam (typically the lowest scan of the KR) reaches almost 2.5 km above sea level 150 km away from the radar. Kwajalein does not have enough reliable gauges to adjust the range dependency of the radar according to gauge measurements. Therefore, to estimate this effect we have calculated the most probable values of the dBZ difference between the lowest elevation angle and the surface for both convective and stratiform precipitation.

The reflectivity profile correction values are derived by a procedure similar to that of Vignal et al. (2000). The method is applied to 1313 three-dimensional volumes of data obtained by the KR between August 1998 and January 2001. The data volumes are all those obtained by the KR during TMI overpass times during this period. These volumes constitute a randomly selected sample of sufficient size to represent a wide range of conditions at Kwajalein. The profiles include radar data only out to 50 km from the radar to ensure sufficient vertical resolution and coverage down to the 0.5-km altitude. The volumes were interpolated (using SPRINT) to 0.5 km in the vertical and 2 km × 2 km in the horizontal. Convective and stratiform pixels are identified in the 2A54UW product (Fig. 3). Table 4 contains the reflectivity difference between the 0.5-km level and the indicated beam height as determined from this dataset for both convective and stratiform regions. These values are the modes for the entire 1313 volume dataset. Because the KR data begin at 0.5 km AMSL, the curve was extrapolated to the surface from 0.5 km using the slope between 0.5 and 1 km. These profiles are generally consistent with vertical profiles of reflectivity derived for convective and stratiform echoes by previous investigators (e.g., Zipser and Lutz 1994; DeMott and Rutledge 1998; Steiner and Houze 1998).

We apply the vertical profile correction to the height of the center of the beam of the lowest elevation scan for each radar pixel. From this height and with the classification of the pixel as convective or stratiform, the appropriate correction value is obtained and added to the reflectivity in the pixel to obtain the best estimate of the surface reflectivity at that horizontal pixel. After applying the vertical profile correction, an appropriate $Z–R$ relation is then applied to this vertical profile–corrected map to yield the associated rain maps. For the map representing the ''low'' estimate, the stratiform correction value is used for all echo regions. For the ''high'' estimate map, the convective correction value is used for all echo regions.

As an independent test of our vertical profile corrections we have employed data from an S-band vertical profiler deployed at Legan (see map in Fig. 2) from September 1999 to December 2000. The vertical profiles of reflectivity in convective and stratiform regions passing over the profiler are shown in Fig. 8. The convective/stratiform determination is based on the KR classification in the pixel above the profiler. The plotted values are expressed as dBZ differences from the disdrometer-measured reflectivity at the surface. The lowest useful level from the profiler is 400 m, similar to the KR data. Future observational studies need to determine the reflectivity profile below the 500-m level. Horizontal bars in Fig. 8 indicate the percentiles of the dataset. The median values are comparable to the modal values and are shown as dashed profiles. The median values can be compared with the KR-derived curves, shown as thick, solid lines.

Figure 8 indicates that the KR-derived vertical profile corrections fall well within the statistical distributions of the profiler observations and agree well with the profiler's median values, especially in the convective case. There is a slight offset between the KR and profiler stratiform profiles that could be related to our extrapolation near the surface or to the environmental conditions over Legan.

7. Uncertainty in the $Z–R$ derived from drop size distribution data

The drop size distribution of the rainfall sampled by radar varies. Therefore, the rain rate estimated from reflectivity is always an educated guess, based on the statistics of the drop size spectra that occur in the region of the radar site. How the statistics of the drop size spectra should be applied to make a guess of the rain rate depends on how the radar data are to be applied. Every measurement of the drop size spectrum implies a relationship between the rain rate R and the Rayleigh-scattering properties of the drops (i.e., their reflectivity Z at the wavelengths of weather radar). The best guess of the instantaneous rain rate is derived from the modal value of the rain rate associated with a given Z. The best estimate of the net rain accumulation over a long time period and area is derived from the mass-weighted mean of the number distribution of the rain rate associated with a given Z. Because the rain rate over tropical oceans tends to be lognormally distributed, the mode, mean, and mass-weighted means may differ substantially. Hence, we must choose the $Z–R$ relation based on the application we have in mind. Because the goal
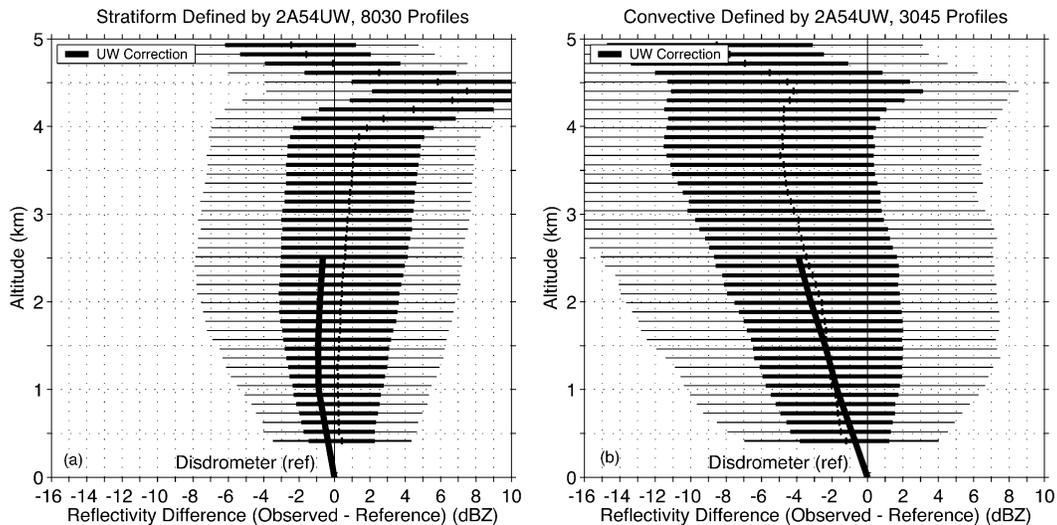
FIG. 8. S-band profiler observations from Legan Island, Kwajalein atoll, for September 1999–December 2000 plotted as the reflectivity difference from the disdrometer reference reflectivity at the surface. Dashed lines represent the median values, thick horizontal bars represent the 25%–75% percentile data range, and thin horizontal bars represent the 10%–90% percentile data range. Data are separated into (a) stratiform and (b) convective by the KR horizontal classification. The climatological stratiform and convective modal reflectivity profile observed by the Kwajalein scanning radar are overlaid in thick black.

of TRMM is to produce accurate climatological rain accumulations over large time and space scales (Simpson et al. 1988), we have chosen a Z–R relation that gives the best time–area integrated climatological results. This relation could differ from that which gives the best instantaneous rain mapping.

To derive the Z–R that will give the best climatological rainfall results for Kwajalein, we use drop size data collected by a Joss–Waldvogel disdrometer at Kwajalein in the wet seasons of 1999 [the year of the Kwajalein Experiment (KWAJEX); Yuter et al. 2004, manuscript submitted to J. Appl. Meteor.; http//www.atmos.washington.edu/kwajex/] and 2000. We compare two sets of data: the R values calculated directly from the drop size distribution (DSD; i.e., calculated R) and the R values derived using the Z–R relation with the Z calculated from the DSD as input (i.e., derived R).

The procedure for determining the best estimate of the instantaneous rain rate would be to minimize error in an individual sample (i.e., one pixel in one instantaneous map or 1 disdrometer sample). The associated metric would be a root-mean-square error between the calculated and derived R, and so the "best" Z–R for this application has the lowest root-mean-square error. We did not do this because we seek the Z–R that will produce the best climatological rain accumulation over the Kwajalein region. Instead, we minimized error in rain accumulation over many samples. The associated metric weights heavier rain rates more as they contributed more to the accumulation. We examined the ratio of the accumulation of the calculated Rs and the accumulation of the derived Rs. The best Z–R relation has a ratio of 1.

For the Z–R relation we use the standard form $Z =$ $aR^{1.5}$. Use of a fixed exponent was proposed by Smith and Joss (1997) and was tested extensively by Doelling et al. (1998) and Steiner and Smith (2000). To obtain values for the coefficient a, we examined the disdrometer data collected in the 1999 and 2000 wet seasons and arrived at the best values of the coefficient a for each wet season independently and for the two wet seasons treated as one large dataset. This superset had 13 153 1-min rain samples. We accumulated these into consecutive 10-min subsets to minimize sampling error in the calculation of Z and R (see Smith et al. 1993). To obtain the Z–R we used 891 10-min samples totaling 869 mm of rain. The resulting lower-limit, best-estimate, and upper-limit Z–R relationships are shown in Fig. 9. The lower and upper limits are based on the difference between the 1999 and 2000 datasets. These relations estimate the year-to-year variability of the Z–R relation at Kwajalein as well as can be done from only 2 years of data. The values of a for the low, best, and high estimates are 190, 175, and 160, respectively. (Note that the higher the value is, the lower the rain rate is because of the inverse nature of the Z–R relation.)

There is an additional instrumental uncertainty associated with the Joss–Waldvogel disdrometer, primarily for smaller drops, which may be blocked from detection by ambient noise. It may be inferred from Joss and Gori (1976) that this uncertainty is <9% for a single measurement at a rain rate of 0.5 mm h^{-1} and decreases to negligible for rates over 10 mm h^{-1}. Over large samples of data this effect is further reduced. For the purposes of this paper, we neglect this instrumental uncertainty.

If and when more drop size data are collected at Kwajalein, we may need to refine our high and low estimates
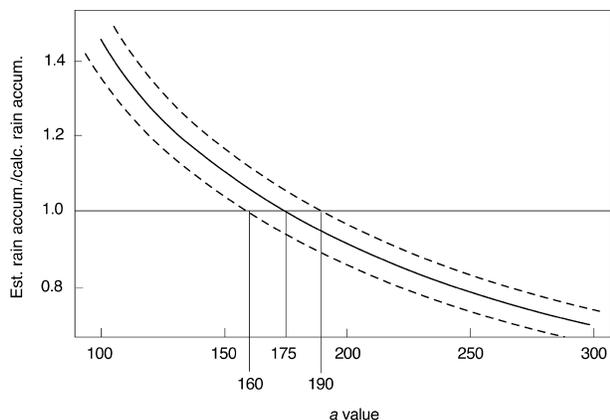
FIG. 9. The best estimate of coefficient *a* to minimize error in rainfall accumulation is determined where the ratio between the estimated rain accumulation using disdrometer-calculated *Z* as input to a *Z–R* relation vs accumulation of the disdrometer-calculated *R* is equal to 1.0. For the merged 1999 and 2000 Joss–Waldvogel disdrometer dataset (solid middle curve), the best coefficient is *a* = 175. Dashed curves show high and low uncertainty estimates where the ratio = 1.0 for *a* = 160 and *a* = 190 in the *Z–R* relation.

FIG. 10. Diagram illustrating the method for filling in gaps in the radar data at Kwajalein. Each tick mark represents a radar volume.

deduced from interannual variability. Based on examination of data from other sites, however, we are reasonably confident in our error bounds and that data from future years will be within them. Application of a *Z–R*-based Mueller and Sims's (1967) collection and analysis of drop size data collected at Majuro (in the Marshall Islands) yields results within the range of our low- and high-estimate *Z–R* relations.

8. Gap-filling uncertainty

Our method for filling data gaps (required for the 3A54UW product, Fig. 3) is illustrated in Fig. 10. For each radar volume during a month, if the time to the next volume is less than 20 min, then that volume's instantaneous rain-rate map is applied to the gap time and the accumulation is added to the monthly accumulation. If the time between two radar observation volumes exceeds 20 min, the gap is filled by interpolation. First, we determine the average rain rate over a time period equal to that of the gap for the times both preceding and following the gap. The lower (higher) rain rate is extrapolated across the gap to provide a low (high) estimate of conditions in the gap. The best estimate of conditions in the gap is obtained by linear interpolation (averaging) of the low and high values across it. If more than 25% of data are missing in a month, the monthly rain map is not created.

As may be obvious, this method becomes more uncertain as the gap size increases. Most of the gaps in the Kwajalein dataset are small enough that the entire rain pattern is unlikely to have changed during the gap time. However, Fig. 11 is an attempt to quantify the uncertainty of the method. For a test month (August 2000), we introduced randomly placed gaps of varying

lengths to see variations in the monthly rain accumulation. One hundred monthly rain maps were created for each gap length of 1, 2, 5, 10, 15, and 24 h. Figure 11 indicates that the standard deviation of the monthly accumulations (shown by the dotted line) is less than or equal to the percent of missing data; for example, a 24-h gap (~3% of missing monthly data) has a standard deviation of ~2%. Monthly accumulations with gaps up to 24 h remain well within ±5% (indicated by the dashed lines) of the observed monthly mean.

9. Kwajalein rainfall climatological results: Monthly rain maps and uncertainties

Figure 12a contains the best-estimate monthly rain map for August 2000, which was a typical rainy season month at Kwajalein in terms of rain amount and the various categories of uncertainty affecting the monthly statistics. The estimated accumulation over the whole
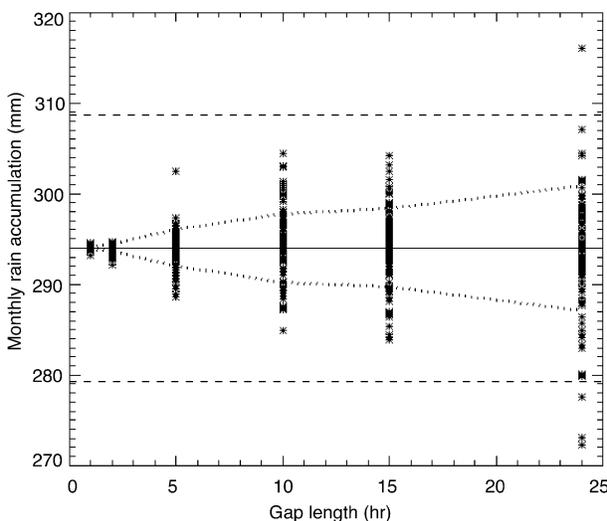
FIG. 11. The spread of monthly rain accumulation for Aug 2000 with randomly placed gaps. Asterisks represent 100 runs with each gap length. The standard deviation of the calculated monthly accumulations is shown by the dotted lines. The solid line indicates the observed rain accumulation for Aug 2000, and the dashed horizontal lines indicate ±5% of the observed monthly mean.
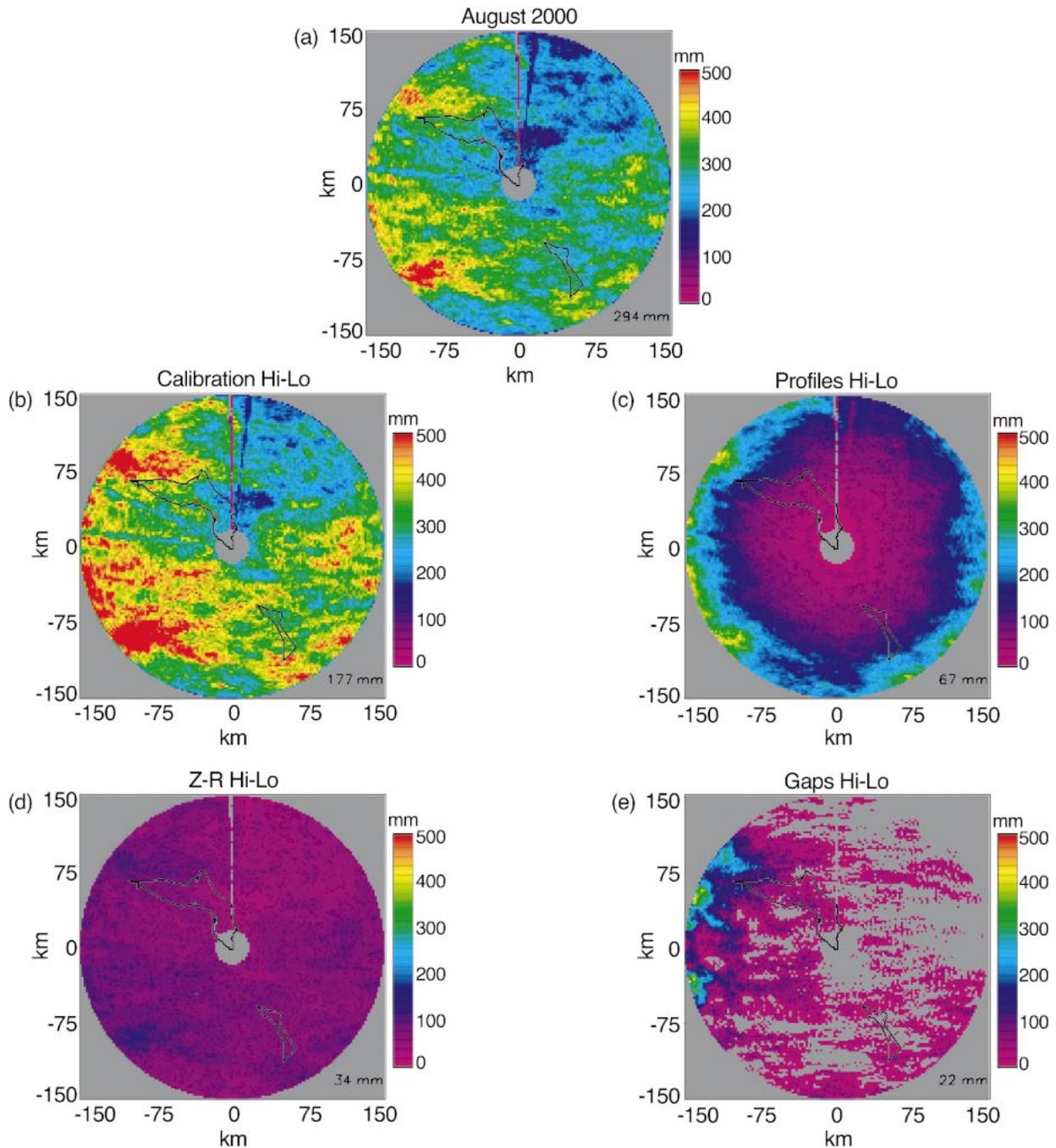
FIG. 12. Rain accumulation for Aug 2000 as shown by the Kwajalein radar. Average amount over the region is shown in the lower-right of each panel. (a) The best estimate for the month. The other panels show the difference between maps computed with (b) low and high estimates of the calibration correction, (c) low and high estimates of the vertical profile correction, (d) low and high estimates of the factor a in the Z–R relationship, and (e) low and high estimates of the echo occurring during gaps in the radar data sampling. The difference map in each panel is computed by using best estimates of all factors except the one considered in that panel.

TABLE 5. Uncertainties in Kwajalein monthly radar-based rain maps for two rainy seasons. The best-estimate monthly rainfall is the areal average of the individual rain accumulation computed at each radar pixel. The ''% data missing'' is the fraction of radar echo observation times for which no data exist or were otherwise corrupt. The uncertainties show the difference between the best estimate of the monthly area average rainfall and the lowest and highest possible values based on physical consideration. Separate ranges of uncertainty are obtained for calibration, vertical profile below the lowest beam, the Z–R relation, and data gaps. Because these uncertainties are based on only three estimates—the best, low, and high (based on physical considerations)—we do not have enough data points to calculate uncertainties based on variance. In the absence of a variance-based estimate of the uncertainty, a simple approach to estimating the total range of uncertainty is to add the four physically based percentage uncertainties on the assumption that these individual uncertainties are independent and equally weighted. This estimate of the total uncertainty is listed in the last column of the table.

Month	Best estimate of the mean rain accumulation in radar area (mm)	% data missing	Calibration uncertainty (%)	Vertical profile uncertainty (%)	Z–R uncertainty (%)	Gap uncertainty (%)	Total uncertainty (%)
Jul 1999	184	4	−30.0	−14.0	−5.3	−1.9	−51.3
			+30.0	+9.9	+6.2	+2.1	+48.1
Aug 1999	158	4	−30.0	−12.9	−5.3	−3.7	−52.0
			+30.0	+10.9	+6.2	+2.8	+49.8
Sep 1999	194	3	−30.0	−13.1	−5.3	−0.8	−49.0
			+30.0	+10.2	+6.2	+0.5	+46.9
Oct 1999	253	6	−30.0	−13.5	−5.3	−2.0	−50.8
			+30.0	+10.1	+6.2	+2.1	+48.3
Nov 1999	282	1	−30.0	−12.1	−5.3	−0.2	−47.6
			+30.0	+11.2	+6.2	+0.2	+47.5
Dec 1999	106	4	−30.0	−13.0	−5.3	−1.3	−49.6
			+30.0	+9.9	+6.2	+1.3	+47.4
Jul 2000	228	4	−30.0	−13.7	−5.3	−1.5	−50.6
			+30.0	+8.6	+6.2	+1.2	+46.0
Aug 2000	294	11	−30.0	−13.8	−5.3	−1.7	−50.8
			+30.0	+8.7	+6.2	+2.3	+47.2
Sep 2000	187	2	−30.0	−14.3	−5.3	−0.4	−50.1
			+30.0	+8.5	+6.2	+0.4	+45.0
Oct 2000	285	2	−30.0	−13.2	−5.3	−0.2	−48.7
			+30.0	+9.2	+6.2	+0.2	+45.5
Nov 2000	194	2	−30.0	−14.0	−5.3	−0.9	−51.0
			+30.0	+9.1	+6.2	+0.9	+47.1
Dec 2000	182	2	−30.0	−13.4	−5.3	−0.3	−49.0
			+30.0	+9.6	+6.2	+0.3	+46.0

area for August 2000 (given in the lower-right of figure panel) is 294 mm. The other panels show the estimated ranges of uncertainty associated with calibration, the vertical profile below the lowest elevation angle, the Z–R relation, and data gaps. The uncertainty is expressed by mapping the difference between the high- and low-estimate maps for each category of uncertainty. This example illustrates that the calibration dominates the uncertainty (Fig. 12b). The net difference between the high- and low-estimate rain accumulations is 177 mm, which is 60% (±30%) of the best estimate of the total rain.

Table 5 lists the ranges of uncertainty for the Kwajalein monthly radar-based rain maps for two rainy seasons. As discussed in sections 5–8, the ranges of uncertainty shown in Table 5 for calibration, the vertical profile below the lowest beam, the Z–R relation, and data gaps reflect three separate estimates of the rain rate (best, low, and high), as deduced from physical considerations. The last column of the tables lists the total uncertainty. The four sources of uncertainty appear to be independent, and the net uncertainty ideally should be obtained by adding variances. However, because we only have three estimates, we do not have enough in-

formation to calculate a meaningful variance. In the absence of a variance-based estimate of the uncertainty, a simple approach to estimating the total range of uncertainty is simply to add the four physically based percentage uncertainties on the assumption that these individual uncertainties are independent and equally weighted.

Table 5 shows that the calibration dominates the uncertainty in all months. The estimated overall uncertainty is about ±50%, with calibration accounting for ±30%. The second greatest uncertainty is the vertical profile of reflectivity below the lowest elevation angle (Fig. 12c). The range between the high- and low-estimate accumulations over the radar area is 67 mm (~±10%); however, this amount is distributed nonuniformly over the area of radar coverage. The amount of uncertainty is much greater at long range. The vertical-profile uncertainty is the only one of our categories of uncertainty that has range dependence.

The magnitude of the uncertainty associated with the Z–R relation (Fig. 12d) is small in comparison with the uncertainties associated with calibration and vertical profiles. The net accumulation difference between high- and low-estimate rain maps is only 34 mm (~±5%) for
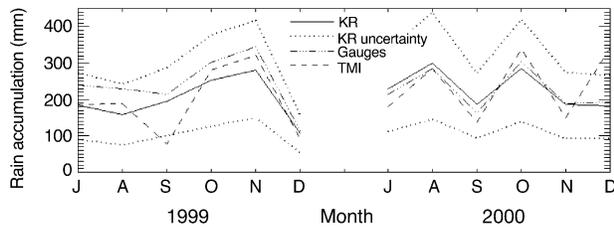
FIG. 13. Solid curve shows the monthly rain amount from the KR over the KR area for two rainy seasons. Dotted lines show the uncertainty in KR monthly rain amount. The other curves show the monthly rain amounts estimated by the TMI and the atoll rain gauges.

the $Z–R$ uncertainty. The uncertainty associated with the $Z–R$ relation is uniform over the area of radar coverage. Sometimes the $Z–R$ relation is treated as an empirical relation between radar measurements and surface rain measurements, and in doing so it is suggested that the $Z–R$ relation should be range dependent (e.g., Rosenfeld et al. 1993). In that empirical approach, range dependency originates in the increase of the height of the lowest elevation scan with range, which we have isolated and treated separately (section 5). Because we treat the $Z–R$ relation physically, that is, as a relationship between two moments (Z and R) of the drop size distribution, $Z–R$ is a property only of the characteristic drop size distribution (section 7). The $Z–R$ percentage uncertainty is, therefore, constant across the area of radar coverage.

The KR was missing 11% of data in August 2000, with a difference of 22 mm ($\sim \pm 2\%$) between the high- and low-estimate maps. Over two rainy seasons listed in Table 5, the percentage of missing maps ranged from 2% to 11% (Table 5). In general, the uncertainty associated with gaps in the monthly dataset (Fig. 12e) was the smallest in terms of overall rain accumulation. However, as illustrated by Fig. 12e, the gap uncertainty can be distributed in space in a very nonuniform pattern, which depends entirely on what echo pattern existed when the data gaps occurred. It might be tempting to correct the monthly accumulation pattern with a uniform factor based on the percentage of maps that are missing. However, this could be in serious error because of the nonuniformity of echoes in space and time. Although the gap uncertainty was small in the monthly maps described in Table 5, the data-gap uncertainty becomes greater, and possibly the dominant uncertainty, for shorter time periods that might be used in short-term forecasting applications.

10. Comparison of KR with TMI and rain gauges

The time series of monthly rain accumulation at Kwajalein, as indicated by our best-estimate KR rain maps, is shown in Fig. 13 (solid curves). Also shown is the net range of uncertainty based on the KR low- and high-estimate maps for each month (dotted curves). The low-

and high-estimate curves indicate the envelope of estimated uncertainty of the KR rain maps.

A primary goal of the work reported in this paper is to provide ground validation rain maps for satellite passive microwave rain estimates over the tropical oceans. The TMI curve in Fig. 13 gives a monthly accumulation estimated from the passive microwave sensor on the TRMM satellite for the months of our KR time series. The TMI rain amounts were calculated using version 5 of the TRMM 2A12 product modified to consider the entire Kwajalein validation area as ocean.[2] TMI data are included for all the overpasses of the KR area during this time period. With only ~ 2 overpasses per day, and with a low probability that a given overpass will have much rain in it because of the natural intermittency of precipitation, the TMI monthly amounts are based on a very limited sample compared to the continuous sampling of the KR. Hence, sampling fluctuations are expected in the TMI data. Overall, the TMI estimates are within a few percent of the KR amounts. Month-to-month variations can be $\sim \pm 25\%$ with major sampling fluctuations most likely the result of sampling in September 1999 and December 2000.

The monthly average of atoll rain gauges also agrees reasonably well with the KR data, especially in the rainy season of 2000. Recall that the gauges are *not* used to calibrate the KR. While the gauges are too few to constitute an a priori basis for calibrating the KR, they do serve as a useful a posteriori check on the PR-based calibration.

11. Conclusions

This study has overcome the challenge of producing a long-term three-dimensional quantitative radar dataset for an ocean site lacking an extensive rain gauge network. The reflectivity fields of the KR have been calibrated with the help of the precipitation radar on the TRMM satellite, which provides a stable calibration standard. The few rain gauges available on the atoll then serve as a posteriori consistency checks but play no role in the calibration adjustments. A simple, quick, and effective method for making the PR-based calibration adjustments to the KR is to require that the area covered by echo be consistent between the KR and PR. In addition, we apply a correction for the vertical profile of reflectivity below the lowest elevation angle, which is a significant correction at longer ranges and is often ignored outside of mountainous regions. This profile is the primary range-dependent correction. Often the range dependence is incorporated into a completely empirical $Z–R$ relation relating radar measurements to gauge measurements. We treat $Z–R$ as a physical relationship con-

---

[2] The version-5 TMI algorithm classified about one-half of the Kwajalein area as coastal (Kummerow et al. 2001). Version 6 will reclassify the entire Kwajalein region as ocean, as we have done in this paper.
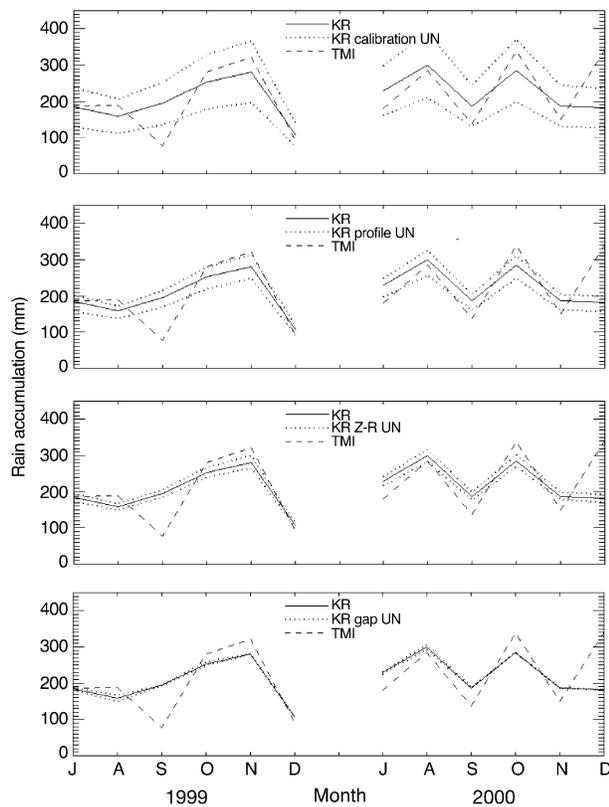
FIG. 14. Same as Fig. 13, except that the KR data are compared only with TMI and the sources of uncertainty are expressed individually. The dotted lines show the range associated with each source of uncertainty.

necting the Z and R moments of the drop size distribution; it is based solely on disdrometer data collected at Kwajalein. We correct for gaps in the data by linearly averaging the data reported on either side of a gap.

By treating each of the above steps in the production of rain maps separately, we isolate the sources of uncertainty associated with the rain maps, which is not possible if the reflectivity is simply correlated with gauge data at various ranges from the radar. By isolating each source of uncertainty, we are able to quantify each source and determine where the greatest uncertainty arises. In the case of the Kwajalein radar, the basic instrument calibration is the greatest source of uncertainty. The archived UW radar data product set for Kwajalein includes these estimated uncertainty fields in addition to the basic rain maps and a full set of three-dimensional reflectivity fields.

In the monthly rain maps based on the Kwajalein radar, the estimated overall uncertainty of the atoll-based radar maps is $\sim\pm50\%$ (last column of Table 5, Figs. 13 and 14). The calibration uncertainty, roughly estimated at $\sim\pm2$ dBZ, accounts for an uncertainty of $\sim\pm30\%$ in monthly rain amounts. The next largest uncertainty is associated with the estimation of the low-altitude vertical profile of reflectivity, which accounts

for $\pm10\%$–15% of the total uncertainty. The Z–R relationship accounts for about $\pm5\%$, and data gaps account for $\pm<2\%$ of the estimated total uncertainty. Efforts to improve the calibration need to focus on the instrument calibration. Improvements could come from equipment upgrades and/or techniques based on polarimetry, which is now operational on the KR.

With the uncertainty fields provided for the Kwajalein rain maps, it is possible to use the radar rain maps as a validation dataset for satellite-based rain maps, especially those from passive microwave sensors on TRMM, NASA's Earth Observing System *Aqua,* and future satellites. We have provided an example of such a comparison with the TRMM Microwave Imager data. The TMI rain maps agree with the KR within the ranges of uncertainty determined by our methodology. If the calibration of the KR were to be improved, these comparisons could be much more precise.

In addition to rain map comparisons, the calibrated KR reflectivity fields can be used in other ways to improve the interpretation of satellite data. Because the KR fields have been calibrated to be consistent with the PR, the KR can be used to assess weaker echo aspects missed by the PR. The weaker echo seen by the KR allows the full echo structure to be seen. The 17-dBZ minimum detectable echo seen by the PR often vastly underestimates both the actual horizontal extent of very light rain and the vertical extent of echoes, whose actual heights are usually determined by less reflective ice particles at the upper levels. The KR fields can also be used for ongoing evaluation of the attenuation corrections applied to the PR. Last, radar echo climatologies compiled from the PR for tropical regions can be anchored to ground-based echo climatologies derived from the KR.

The overall success of the TRMM satellite indicates that satelliteborne radars will continue to fly on satellites well into the future. The KR serves as a prototype for how these future satellite radars can be used in conjunction with ground-based radar. The relationship of the ground radar to the satellite radar need not be independent. As we have shown, the satellite radar can serve as the calibration standard that allows the ground-based radar at an ocean site devoid of a rain gauge network to produce a useful dataset for validation of passive microwave sensors (e.g., Kim et al. 2004), and the more sensitive and continuous measurements of the KR can extend the usefulness of satellite radars by filling in information in space and time not sensed by the satellite radars.

APPENDIX

UW Quality-Control Algorithm

The University of Washington (UW) quality-control (QC) algorithm automatically removes nonmeteorological echo from polar coordinate radar data. We have applied this algorithm at radar sites in different regions. In this appendix, we will consider only the application of the algorithm at Kwajalein. At Kwajalein, the major types of nonmeteorological echo are ground clutter, sea clutter, and second-trip echoes (Rinehardt 1997), which are all removed by the UW QC algorithm. Data removed from the scans are indicated by setting the identified points to a value of missing data. There are 16 inputs to the UW QC algorithm. These parameters vary from place to place and must be set for any individual radar. The input values for Kwajalein data are listed in Table A1.

The KR is a magnetron-based radar, for which the signal quality index (SQI; see Rinehart 1997, p. 113) is available. We use the SQI to filter out second-trip echoes. The first step of the quality-control algorithm takes advantage of the SQI-filtered radial velocity data (when available) to delete second-trip echoes present in the reflectivity field. For each range gate, if the velocity has not been filtered out by the SQI value, and it is within prescribed boundaries, the corresponding reflectivity value remains unchanged. Otherwise, the reflectivity value is set to ''missing data.''

The next step of the algorithm examines the texture of the reflectivity field. It is assumed that the data are collected in a ''volume'' consisting of a series of constant elevation angle scans. The volume is processed starting from the highest elevation angle and ending with the lowest elevation angle. First, two simple ground clutter removal steps are applied. 1) All echoes within a specified range of the radar are deleted. For Kwajalein, ground clutter from nearby towers and buildings is so pervasive that all echoes within 17 km are removed. 2) For sweeps below 2.0° in elevation, a clutter map is applied. For Kwajalein, the clutter map was defined based on locations of stationary, persistent echo for periods when little to no precipitation was present. All echoes falling within ±0.75° in azimuth and ±2 range gates of a clutter point are removed. If the radar volume consists of only one sweep, the UW QC algorithm is complete at this point.

The remaining portion of the texture step of the algorithm examines the 9 × 9 pixel window around every range gate. If the reflectivity value at any gate in the neighborhood (excluding the center gate) is greater than

TABLE A1. Input parameters for UW QC algorithm as applied to the Kwajalein radar.

Parameter	Value
1) Input file name (universal format)	
2) Output file name (universal format)	
3) Boundary level (BL) (km)	0.90
4) Freezing level (FL) (km)	4.90
5) Dielectric flag (on or off)	Off
6) dBZ threshold value below BL (dBZ)	18
7) dBZ threshold value from BL to 1 km above BL	12
8) dBZ threshold value above BL + 1.1 km and below FL	10
9) Max dBZ difference allowable between base and second tilt	35
10) Flag to apply pixel-above test between second and third tilts (0/1)	0
11) SQI filter flag (on or off)	On
12) Max range to apply filter-above test on lowest tilt (km)	40
13) Max radius from radar to unconditionally delete echo (km)	17
14) Name of clutter file	
15) Sweep to treat as lowest tilt (counting starts at 0; for circumstances where the SQI filter cannot be applied, this may be set to nonzero)	0
16) Save polarimetric fields flag (on or off)	Off

or equal to a specified reflectivity threshold (which is a function of height), the value of the center gate is kept; otherwise, its value is set to missing data. Nine by nine was chosen as the optimal grid size after comparing grids ranging from 5 × 5 to 21 × 21 at various reflectivity thresholds. In general, the smaller grids take out too much of the storm edges, while the larger grids take longer to run through the quality control and leave in too many unwanted low-reflectivity pixels.

The set of reflectivity thresholds used in the texture processing are determined empirically. Ground clutter and other abnormal phenomena are seen mainly in the lowest elevation scans. Therefore, a higher reflectivity threshold is necessary for the removal of a near-surface nonprecipitation echo than for an echo at higher altitudes. Three reflectivity thresholds are determined for each of three height regions: ground to boundary layer top, boundary layer top to boundary layer top plus 1.1 km, and from that height to the 0°C level. The texture algorithm is not applied to data at altitudes higher than the 0°C level, except that all of the data in the lowest tilt are always examined whether they are above 0°C or not. At Kwajalein, the 0°C level is always at about 5 km, as it is throughout the Tropics.

For the lowest elevation scan, for all bins within an input range (for Kwajalein, this is 40 km), another step is applied to remove sea clutter before the main texture step described above. Sea clutter is identified using a vertical continuity test. The echo in the second-to-lowest elevation scan is dilated (spread over a wider horizontal window, 3 × 3 pixels around the echo of interest) using a 3 × 3 window. The dilation ensures that vertically sheared echoes are not misidentified as sea clutter. Ech-
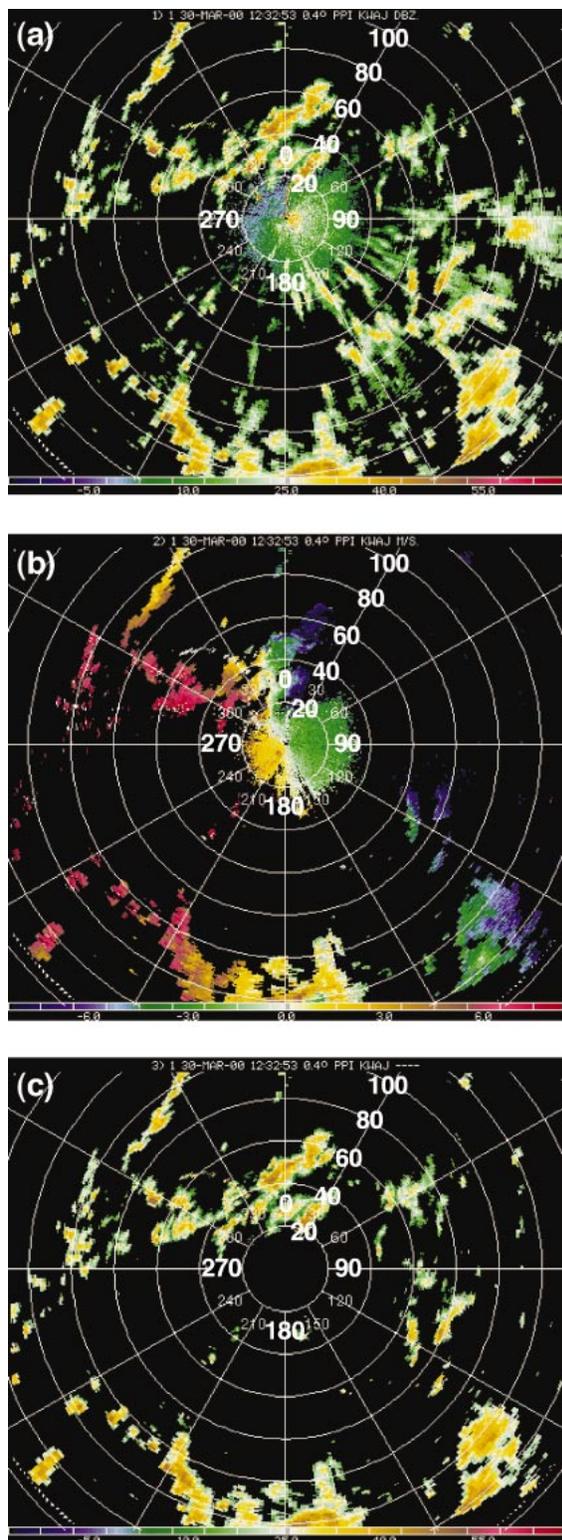
FIG. A1. Low-elevation scan of the KR at 1232 UTC 30 Mar 2000: (a) reflectivity without quality control, (b) radial velocity filtered by SQI, and (c) reflectivity with quality control.

oes that appear in the lowest elevation scan, but have no corresponding echo in the dilated version of the second-to-lowest elevation scan, are removed. In addition to sea clutter removal, this step of the algorithm also removes areas of low-reflectivity nonprecipitation echo and isolated high-reflectivity ground clutter and anomalous propagation (AP), while preserving the low-reflectivity storm edges.

The third part of the algorithm attempts to remove any remaining AP by examining an areal average difference in reflectivity with height. This part of the algorithm is applied after the texture test has been applied to the entire volume. The 3×3 window averages of the second-to-lowest elevation scan and the lowest elevation scan are computed. If the difference between the average reflectivity at a point in the lowest elevation scan and the point directly above in the next-to-lowest elevation scan is more than a specified threshold (normally between 25 and 35 dBZ), then the values of both points are set to missing data. This method removes the middle of strong AP in multiple tilts but often leaves the edges of a strong AP region intact.

Generally AP does not occur at Kwajalein, and so this aspect of the UW QC algorithm is not relevant. The UW QC algorithm has been applied to various regimes, and the performance of the algorithm in cases of AP is available upon request. An example of UW QC results for Kwajalein is shown in Fig. A1. In this example, second-trip echoes are removed by applying the SQI-filtered radial velocity field as a mask on the reflectivity field. All of the ground and sea clutter has been removed. Most of the ground and sea clutter has been taken out by deleting the 17-km circle of echo around the radar, but individual pixels of persistent clutter echo at farther ranges, especially from certain towers, have also been removed.

REFERENCES

Anagnostou, E. N., C. A. Morales, and T. Dinku, 2001: The use of TRMM precipitation radar observations in determining ground radar calibration biases. *J. Atmos. Oceanic Technol.,* **18,** 616–628.

Barnes, S. L., 1980: Report on a meeting to establish a common Doppler-radar data exchange format. *Bull. Amer. Meteor. Soc.,* **61,** 1401–1404.

Bolen, S. M., and V. Chandrasekar, 2000: Quantitative cross validation of space-based and ground-based radar observations. *J. Appl. Meteor.,* **39,** 2071–2079.

Churchill, D. D., and R. A. Houze Jr., 1984: Development and structure of winter monsoon cloud clusters on 10 December 1978. *J. Atmos. Sci.,* **41,** 933–960.

DeMott, C. A., and S. A. Rutledge, 1998: The vertical structure of TOGA COARE convection. Part II: Modulating influences and implications for diabatic heating. *J. Atmos. Sci.,* **55,** 2748–2762.

Doelling, I. G., J. Joss, and J. Riedl, 1998: Systematic variations of *Z-R* relationships from drop-size distributions measured in northern Germany during seven years. *Atmos. Res.,* **47–48,** 635–649.

Iguchi, T., T. Kozu, R. Meneghini, J. Awaka, and K. Okamoto, 2000: Rain-profiling algorithm for the TRMM precipitation radar. *J. Appl. Meteor.,* **39,** 2038–2052.

Joss, J., and E. G. Gori, 1976: The parameterization of raindrop size distributions. *Riv. Ital. Geofis.,* **3,** 275–283.

——, and A. Waldvogel, 1990: Precipitation measurements and hydrology. *Radar in Meteorology: Battan Memorial and 40th Anniversary Radar Meteorology Conference,* D. Atlas, Ed., Amer. Meteor. Soc., 577–606.

——, and Coauthors, 1998: *Operational Use of Radar for Precipitation Measurements in Switzerland.* vdf Hochschulverlag AG an der ETH, 108 pp.

Kidder, S. Q., and T. H. Vonder Haar, 1995: *Satellite Meteorology: An Introduction.* Academic Press, 466 pp.

Kim, M.-J., J. A. Weinman, and R. A. Houze Jr., 2004: Validation of maritime rainfall retrievals from the TRMM microwave radiometer. *J. Appl. Meteor.,* **43,** 847–859.

Kozu, T., and Coauthors, 2001: Development of precipitation radar onboard the tropical rainfall measuring mission satellite. *IEEE Geosci. Remote Sens.,* **39,** 102–116.

Kummerow, C., W. Barnes, T. Kozu, J. Shiue, and J. Simpson, 1998: The Tropical Rainfall Measuring Mission (TRMM) sensor package. *J. Atmos. Oceanic Technol.,* **15,** 808–816.

——, and Coauthors, 2001: The evolution of the Goddard profiling algorithm (GPROF) for rainfall estimation from passive microwave sensors. *J. Appl. Meteor.,* **40,** 1801–1820.

Marks, D. A., and Coauthors, 2000: Climatological processing and product development for the TRMM Ground Validation Program. *Phys. Chem. Earth,* **25B,** 871–875.

Mohr, C. G., and R. L. Vaughan, 1979: An economical procedure for Cartesian interpolation and display of reflectivity factor data in three-dimensional space. *J. Appl. Meteor.,* **18,** 661–670.

Mueller, E. A., and A. L. Sims, 1967: Raindrop distributions at Majuro Atoll, Marshall Islands. Atmospheric Sciences Laboratory, U.S. Army Electronics Command Tech. Rep. ECOM-02071-RR1, 93 pp.

Rinehart, R. E., 1997: *Radar for Meteorologists.* Rinehart Publishing, 428 pp.

Rosenfeld, D., D. B. Wolff, and D. Atlas, 1993: General probability-matched relations between radar reflectivity and rain rate. *J. Appl. Meteor.,* **32,** 50–72.

Schumacher, C., and R. A. Houze Jr., 2000: Comparison of radar data from the TRMM satellite and Kwajalein oceanic validation site. *J. Appl. Meteor.,* **39,** 2151–2164.

——, and ——, 2003a: The TRMM precipitation radar's view of shallow, isolated rain. *J. Appl. Meteor.,* **42,** 1519–1524.

——, and ——, 2003b: Stratiform rain in the Tropics as seen by the TRMM precipitation radar. *J. Climate,* **16,** 1739–1756.

Simpson, J., R. F. Adler, and G. R. North, 1988: A proposed Tropical Rainfall Measuring Mission (TRMM) satellite. *Bull. Amer. Meteor. Soc.,* **69,** 278–295.

Smith, P. L., and J. Joss, 1997: Use of a fixed exponent in ''adjustable'' *Z-R* relationships. Preprints, *28th Conf. on Radar Meteorology,* Austin, TX, Amer. Meteor. Soc., 254–255.

——, Z. Liu, and J. Joss, 1993: A study of sampling variability effects in raindrop size observations. *J. Appl. Meteor.,* **32,** 1259–1269.

Steiner, M., and R. A. Houze Jr., 1998: Sensitivity of monthly three-dimensional radar-echo characteristics to sampling frequency. *J. Meteor. Soc. Japan,* **76,** 73–95.

——, and J. A. Smith, 2000: Reflectivity, rain rate, and kinetic energy flux relationships based on raindrop spectra. *J. Appl. Meteor.,* **39,** 1923–1940.

——, R. A. Houze Jr., and S. E. Yuter, 1995: Climatological characterization of three-dimensional storm structure from operational radar and rain gauge data. *J. Appl. Meteor.,* **34,** 1978–2007.

Stephens, G. L., 1994: *Remote Sensing of the Lower Atmosphere: An Introduction.* Oxford University Press, 523 pp.

Vignal, B., G. Galli, J. Joss, and U. Germann, 2000: Three methods to determine profiles of reflectivity from volumetric radar data to correct precipitation estimates. *J. Appl. Meteor.,* **39,** 1715–1726.

Wilheit, T. T., 1986: Some comments on passive microwave measurement of rain. *Bull. Amer. Meteor. Soc.,* **67,** 1226–1232.

——, A. T. C. Chang, M. S. V. Rao, E. B. Rodgers, and J. S. Theon, 1977: A satellite technique for quantitatively mapping rainfall rates over the oceans. *J. Appl. Meteor.,* **16,** 551–560.

Yuter, S. E., and R. A. Houze Jr., 1997: Measurements of raindrop size distributions over the Pacific warm pool and implications for *Z–R* relations. *J. Appl. Meteor.,* **36,** 847–867.

Zipser, E. J., and K. R. Lutz, 1994: The vertical profile of radar reflectivity of convective cells: A strong indicator of storm intensity and lightning probability? *Mon. Wea. Rev.,* **122,** 1751–1759.